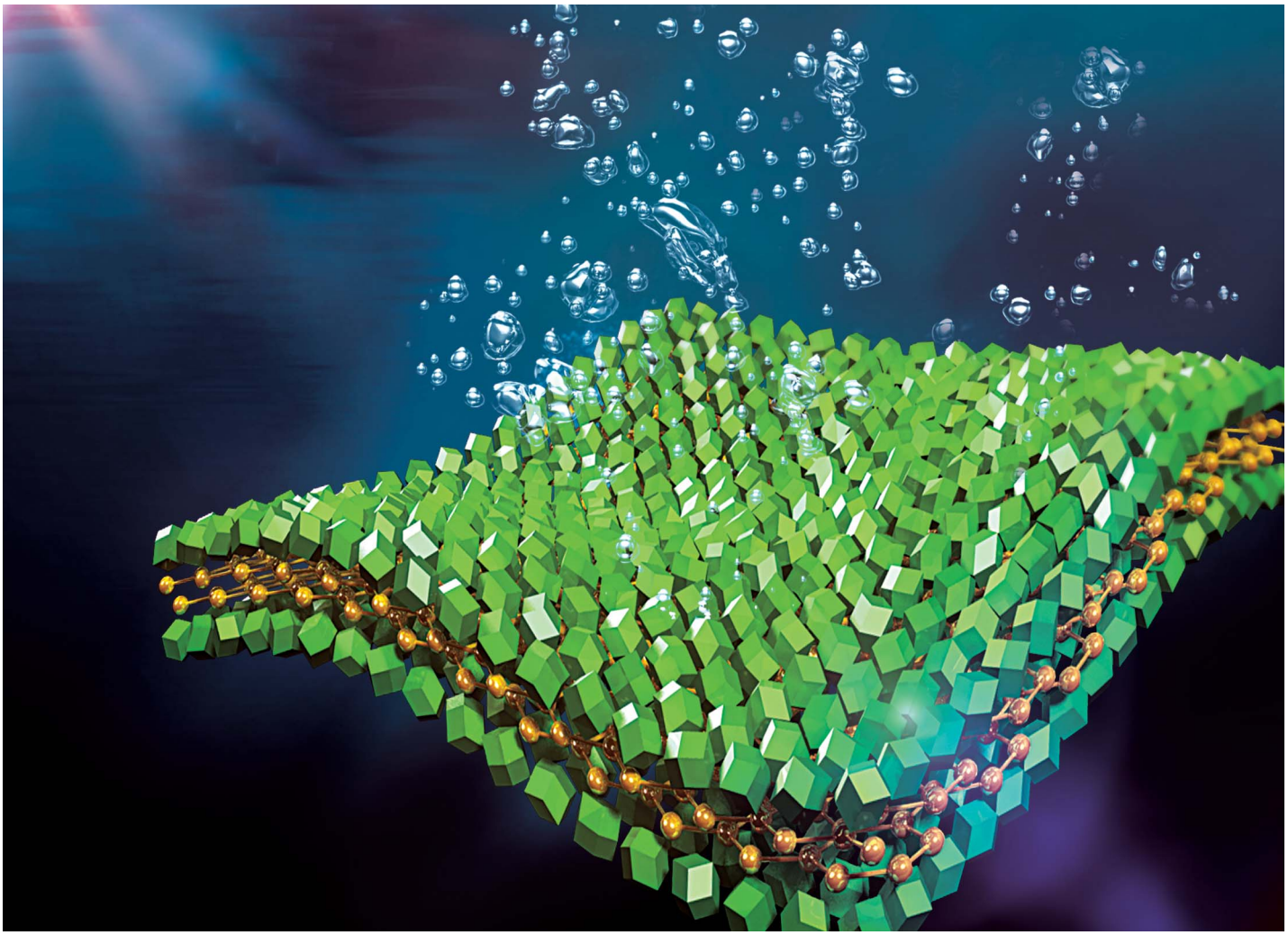

Showcasing work from the groups of Zhao and Wang and the university of Xi'an Jiaotong University and Monash University.

Graphene oxide/core–shell structured metal–organic framework nano-sandwiches and their derived cobalt/N-doped carbon nanosheets for oxygen reduction reactions

Wei and co-authors have developed a metal–organic framework (MOF) seed-mediated deposition route to synthesize graphene oxide/core–shell structured MOF nano-sandwiches and cobalt/N-doped carbon electrocatalysts. This work was jointly carried out at Xi'an Jiaotong University and Monash University. Prof. San Ping Jiang and Prof. Zhanfeng Zheng are acknowledged for their collaboration with this work.

As featured in:

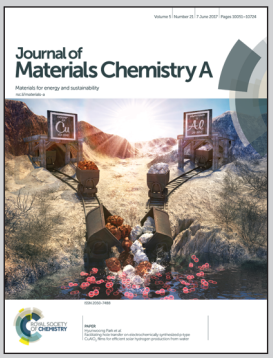

See Yongxi Zhao, Huanting Wang *et al.*, *J. Mater. Chem. A*, 2017, **5**, 10182.

ROYAL SOCIETY OF CHEMISTRY

rsc.li/materials-a

Registered charity number: 207890

Journal of Materials Chemistry A

PAPER

View Article Online
View Journal | View Issue

Cite this: J. Mater. Chem. A, 2017, 5, 10182

Graphene oxide/core–shell structured metal–organic framework nano-sandwiches and their derived cobalt/N-doped carbon nanosheets for oxygen reduction reactions†

Jing Wei,[ab] Yaoxin Hu,[b] Yan Liang,[b] Biao Kong,[c] Zhanfeng Zheng,[d] Jin Zhang,[e] San Ping Jiang,[e] Yongxi Zhao*[a] and Huanting Wang*[b]

A metal–organic framework (MOF) seed-mediated deposition route is developed to synthesize MOF/graphene oxide (GO)/MOF nano-sandwiches with core–shell structured MOF (*i.e.* ZIF-8@ZIF-67) crystals uniformly distributed on GO. Due to the well controllable growth rate, ZIF-8 seeds are first deposited on GO. Then, ZIF-67 species are selectively deposited on the surface of ZIF-8 to form core–shell structures owing to their similar crystal structure and unit cell parameter. Compared with the direct deposition of ZIF-67 crystals on GO, this MOF seed-mediated synthesis can effectively prevent the over-growth and inhomogeneous distribution of ZIF-67 crystals. The GO/core–shell MOF composites are further demonstrated to be an excellent precursor for cobalt/N-doped carbon nanosheets, which are efficient nonprecious metal catalysts for oxygen reduction reactions, and exhibit a high onset potential (~0.93 V *versus* reversible hydrogen electrode, *vs.* the RHE) and large kinetic current density (~101 mA mg^{-1} at 0.80 V *vs.* the RHE). Such novel carbon materials derived from the core–shell structured MOF also show better catalytic performance than those derived from both GO/ZIF-8 and GO/ZIF-67 prepared under the same conditions. This work offers an alternative strategy to develop MOF-derived carbon-based composites using GO/core–shell structured MOFs as a kind of fresh precursors.

Received 9th January 2017
Accepted 30th March 2017

DOI: 10.1039/c7ta00276a

rsc.li/materials-a

Introduction

Nanoporous carbon materials, especially with heteroatoms (such as nitrogen) doping, have attracted intensive interest due to their thermal and chemical stability, excellent electrical conductivity, high specific surface area and various applications including adsorption and separation, catalysis, energy conversion and storage.[1–13] Recently, metal–organic frameworks (MOFs) have been intensively used as excellent carbon precursors to synthesize nanoporous carbon materials *via* direct carbonization without using auxiliary templates.[14–17] Especially, MOFs assembled from metal nodes and N-rich organic ligands (such as zeolitic imidazolate frameworks, ZIFs, a subclass of MOF) can be converted to nanoporous N-doped carbon with a high N content.[18–21] Furthermore, some metal (such as Fe and Co) nodes could also be incorporated into carbon *via* coordination with nitrogen atoms, resulting in the metal/N-doped carbon materials.[22–26] Such metal/N-doped nanoporous carbons have been regarded as a promising nonprecious metal catalyst with low-cost, high efficiency and excellent durability to replace Pt for the oxygen reduction reaction (ORR), an important electrode reaction with sluggish reaction kinetics in fuel cells and metal–air batteries.[27–32] In addition, combining MOFs with graphene oxide (GO), their derived carbon composites (nanoporous carbon/reduced graphene oxide, rGO) exhibit enhanced electrochemical performance due to the increased electrical conductivity and density of active sites.[33–38] And consequently, various MOF materials have been grown or mixed with GO to prepare MOF/GO composites as a new kind of carbon source. Some of these MOF/GO composites have been explored as carbon precursors for the fabrication of high-performance electrocatalysts for the ORR, oxygen evolution reaction (OER) and hydrogen evolution reaction (HER).[33–38] However, due to the weak interactions between MOF and GO, as well as the fast growth kinetics of the MOF, most of the MOF/GO composites show poorly controllable nanostructures, such as

[a]The Key Laboratory of Biomedical Information Engineering of Ministry of Education, School of Life Science and Technology, Xi'an Jiaotong University, Xi'an, Shaanxi 710049, P. R. China. E-mail: yxzhao@xjtu.edu.cn

[b]Department of Chemical Engineering, Monash University, Clayton, Victoria 3800, Australia. E-mail: huanting.wang@monash.edu

[c]Department of Chemistry, Laboratory of Advanced Materials, Fudan University, Shanghai 200433, P. R. China

[d]State Key Laboratory of Coal Conversion, Institute of Coal Chemistry, Chinese Academy of Sciences, Taiyuan 030001, P. R. China

[e]Fuels and Energy Technology Institute, Department of Chemical Engineering, Curtin University, Perth, WA 6102, Australia

† Electronic supplementary information (ESI) available. See DOI: 10.1039/c7ta00276a

inhomogeneous distributions of MOF particles on the GO and a large crystal size (>50 nm).[33–37] As a result, their synergetic enhancement of catalytic performance is limited due to the inhomogeneous structure.

To fully explore their catalytic activity for the ORR, MOF/GO derived carbon composites should have a nanoporous structure for the fast mass transport, high content of active sites (such as N-doping carbon and M–N–C, M = Fe and Co), high specific surface area for exposing as many as active sites, and excellent electrical conductivity for fast electron transfer. To meet these requirements, one of the most promising nanostructures is an MOF/GO/MOF sandwich-like nanosheet, where MOF crystals should be as small as possible to be uniformly deposited on the GO sheet with high density. The sandwich-like MOF/GO/MOF derived carbon composites will retain the nanosheet morphology due to the protection of the MOF crystal layer during the carbonization process, which is beneficial to the fast mass transport. The rGO obtained from high-temperature carbonization of GO will enhance the electrical conductivity of the composites, which is required for fast electron transfer. Most importantly, the close-packing of MOF nanocrystals on GO can lead to a high-density of active sites distributed on rGO as the active sites are formed by the carbonization of MOF. Recently, the sandwich-like ZIF-8/GO/ZIF-8 composites with ZIF-8 nanocrystals deposited on GO uniformly have been synthesized and further demonstrated to be good precursors for the fabrication of N-doped carbon nanosheets with high catalytic performance for the ORR.[33,38] However, ZIF-8, assembled by using zinc nodes and 2-methylimidazole ligands, cannot provide Fe (or Co) species to fabricate high-performance M–N–C (M = Fe and Co) active sites, resulting in lower catalytic activity than M–N–C (M = Fe, Co)-based catalysts.

ZIF-67, composed of cobalt nodes and 2-methylimidazole ligands, can be converted to porous carbon with an abundance of Co–N–C active sites. It's promising to fabricate high-performance catalysts by depositing ZIF-67 crystals on GO nanosheets to fabricate sandwich-like ZIF-67/GO/ZIF-67 composites as a catalyst precursor. However, due to the weak interactions between ZIF-67 seeds and GO, as well as the fast growth kinetics of ZIF-67, GO has very limited effects to restrict the growth of ZIF-67. As a result, ZIF-67 crystals directly deposited on the GO sheet usually show inhomogeneous distributions and a large crystal size *via* the direct growth route, which would hinder the effective utilization of active sites (Co–N–C) (Fig. 1a).[33,34] It's desirable to develop a method to deposit Co-based MOFs (such as ZIF-67) on GO uniformly for the fabrication of highly efficient electrocatalysts. In addition, several studies have recently proven that the carbon composites derived from bimetallic ZIFs with different ratios of Zn/Co exhibit higher catalytic performance than sole metal-contained MOFs.[39–41] Such bimetallic ZIFs show two kinds of metal ions homogeneously distributed in the framework, which can effectively combine the advantages of carbon derived from ZIF-8 (such as high surface area and high N content) and ZIF-67 (such as high graphitization degree and high content of Co–N–C active sites). The design of novel MOF composites with core–shell structures and tuneable compositions is beneficial for tailoring the properties of the derived catalyst, further improving the catalytic performance. However, there are very few studies using the core–shell structured MOFs, especially the GO/core–shell structured MOF composites, as a carbon precursor for the fabrication of carbon-based electrocatalysts.[42,43]

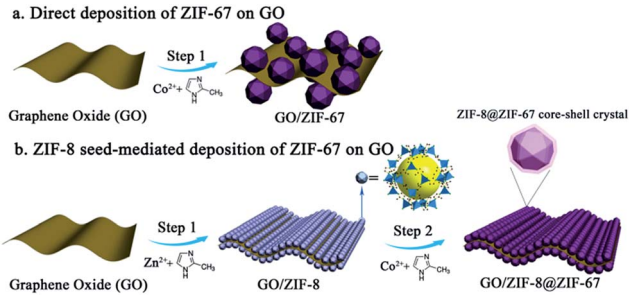

Fig. 1 Comparison of different methods for the synthesis of MOF/GO composites: (a) direct deposition of ZIF-67 on the GO sheet; (b) ZIF-8 seed-mediated deposition of ZIF-67 on the GO sheet.

Herein, we develop a ZIF-8 seed-mediated deposition route to synthesize MOF/GO/MOF sandwich-like nanosheets, where the core–shell structured ZIF-8@ZIF-67 nanocrystals were deposited on GO uniformly (Fig. 1b). This ZIF-8 seed-mediated deposition route includes two steps. First, ZIF-8 seeds are deposited on the GO sheets directly. Due to the strong interactions between the metal clusters from ZIF-8 and the oxygen-containing groups from GO, as well as a moderate crystal growth rate, ZIF-8 can be readily deposited on both sides of the GO sheet to form a ZIF-8/GO/ZIF-8 sandwich-like structure. Then, ZIF-67 crystals are selectively deposited on the surface of ZIF-8 seeds due to the similar crystal structure and unit cell parameter. As a result, the core–shell structured ZIF-8@ZIF-67 crystals are deposited on GO nanosheets uniformly and compactly to form a ZIF/GO/ZIF sandwich-like structure. After further carbonization and the acid etching process, ZIF/GO/ZIF can be converted to cobalt nanoparticles/N-doped porous carbon nanosheets, which exhibit a high onset potential (~0.93 V *vs.* the RHE), large kinetic current density (~101 mA mg^{-1} at 0.80 V *vs.* the RHE) and excellent stability. We further demonstrate that the carbon materials derived from GO/core–shell structured ZIF-8@ZIF-67 composites show better catalytic performance than those from both GO/ZIF-8 and GO/ZIF-67 due to the advanced core–shell structure. As far as we known, it's the first example to use GO/core–shell structured MOF sandwich-like composites as a precursor for the fabrication of advanced carbon materials for electrocatalysis.

Results and discussion

To compare the differences between the direct deposition of ZIF-67 on GO and the ZIF-8 seed-mediated deposition route, ZIF-67 crystals were firstly deposited on GO directly by adding GO solution in the precursors of ZIF-67 (*i.e.* 2-methylimidazole and cobalt nitrate solution). The obtained samples were denoted as GO/ZIF-67. Scanning electron microscopy (SEM) images of GO/ZIF-67 reveal that the crystal size of ZIF-67 is around 80 nm and the crystals are deposited on the GO sheet inhomogeneously (Fig. S1†).

The ZIF-8 seed-mediated deposition method consists of two steps. In the first step, ZIF-8 seeds were deposited on the GO sheet directly by adding GO solution into the precursors of ZIF-8 (2-methylimidazole and zinc nitrate solution). The obtained samples were denoted as GO/ZIF-8. The SEM image of GO/ZIF-8 reveals that ZIF-8 nanocrystals are distributed on the GO sheets uniformly to form a ZIF-8/GO/ZIF-8 sandwich-like structure (Fig. 2a). Although the synthesis method for the deposition of ZIF-8 and ZIF-67 is very similar, dramatically different results are obtained, implying that ZIF-8 crystals are more easily deposited on the GO sheets than ZIF-67. As the main differences between ZIF-67 and ZIF-8 are metal nodes (Co for ZIF-67 and Zn for ZIF-8), the different GO/MOF structures obtained here may be due to the different growth rates of the MOF crystals.

In the second step, ZIF-67 crystals were deposited on the GO/ZIF-8 composites. The obtained samples were denoted as GO/ZIF-8@ZIF-67. The SEM images of GO/ZIF-8@ZIF-67 show that the MOF crystals are distributed on the GO sheet uniformly, which is similar to that of GO/ZIF-8 (Fig. 2b and c), indicating that the deposition process of ZIF-67 doesn't destroy the ZIF/GO/ZIF sandwich-like structure. By comparing the high-resolution SEM images of GO/ZIF-8@ZIF-67 and GO/ZIF-8, the distance between each crystal becomes smaller, revealing the formation of a ZIF-67 shell on the ZIF-8 core (Fig. S2†). In addition, different from GO/ZIF-67, a very few large MOF crystals were observed on GO. The transmission electron microscopy (TEM) images and corresponding element mapping were further investigated. The TEM images of GO/ZIF-8@ZIF-67 further reveal that the MOF crystals are deposited on GO uniformly (Fig. 2d and e). The corresponding element mapping results prove that both Zn and Co species are distributed in the MOF crystals, indicating the successful deposition of ZIF-67 on ZIF-8 seeds (Fig. 2f–j). The overall crystal size of ZIF-8@ZIF-67 obviously decreased compared with that of ZIF-67 directly grown on the GO sheet, indicating that the ZIF-8 seeds could avoid the overgrowth of ZIF-67. Due to the decreased crystal size, more MOF crystals can be deposited on GO, which could obviously increase the density of catalytic active sites for the ORR after carbonization.

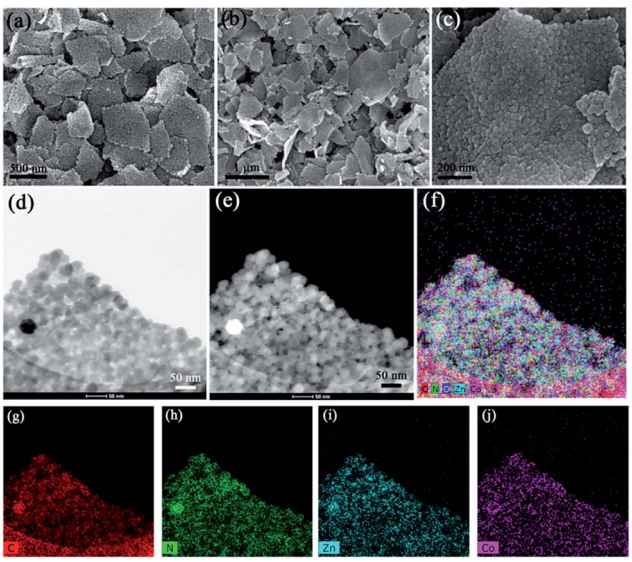

Fig. 2 SEM images of (a) GO/ZIF-8 and (b and c) GO/ZIF-8@ZIF-67 with different magnifications. (d and e) TEM and (f–j) corresponding element mapping images of GO/ZIF-8@ZIF-67.

As the MOF crystals on GO are uniform and no other crystals are deposited separately, we presume that the ZIF-67 is selectively deposited on ZIF-8 to form a core–shell structured ZIF-8@ZIF-67. Due to the similar crystal structure and unit cell parameters between ZIF-8 ($a = b = c = 16.9910$ Å) and ZIF-67 ($a = b = c = 16.9589$ Å),[44,45] ZIF-67 crystals are more prone to grow on the surface of ZIF-8 seeds during the deposition process. Recently, Tang *et al.* have demonstrated that ZIF-67 can be readily grown on ZIF-8 crystals to form ZIF-8@ZIF-67 core–shell crystals.[42] The cobalt ions could be preferentially immobilized on the surface of ZIF-8 seeds through the coordination interactions with 2-methylimidazole ligands on the ZIF-8 surface, followed by the growth of the ZIF-67 shell *via* the interactions between the Co ions and the additive 2-methylimidazole ligands. Following the same principle, ZIF-67 could also be selectively deposited on ZIF-8 seeds with a smaller crystal size (<50 nm) from GO/ZIF-8 composites. The ZIF-8 seeds on GO can mediate the deposition process of ZIF-67, preventing the inhomogeneous deposition and overgrowth of ZIF-67 on the GO sheet. The X-ray diffraction (XRD) patterns of all the GO/MOF and MOF crystals show the same sodalite (SOD) topology with the space group $I\bar{4}3m$, revealing that the crystal structure is well maintained during the deposition process of ZIF-8 and ZIF-67 (Fig. S3†).

The molar ratio of Co to Zn in the core–shell structured ZIF-8@ZIF-67 can be easily adjusted by changing the concentrations of cobalt nitrate methanolic solution during the deposition process. In a typical synthesis process, the concentration of Co^{2+} solution is 0.25 mol L^{-1}. When the concentrations of Co^{2+} solution are 0.0125 and 0.05 mol L^{-1}, the obtained GO/MOF composites are denoted as GO/ZIF-8@ZIF-67-L and GO/ZIF-8@ZIF-67-H, respectively. The SEM images of GO/ZIF-8@ZIF-67-L and GO/ZIF-8@ZIF-67-H show an MOF/GO/MOF sandwich-like nanostructure similar to that of GO/ZIF-8@ZIF-67, indicating that the GO/MOF structure can be easily synthesized in the broad concentrations of Co^{2+} (Fig. S4†). The energy dispersive X-ray spectrum (EDS) results reveal that the molar ratio of Co to Zn is 0.22, 0.45 and 0.98 for GO/ZIF-8@ZIF-67-L, GO/ZIF-8@ZIF-67 and GO/ZIF-8@ZIF-67-H, respectively, implying that such a ZIF-8 seed-mediated deposition approach can efficiently control the deposition amount of ZIF-67 on ZIF-8 seeds by changing the concentrations of the cobalt precursor (Fig. S5†).

When directly depositing ZIF-67 on GO, ZIF-67 materials show a large crystal size and irregular distributions on GO due to the fast growth rate. By contrast, the ZIF-8 mediated deposition method can effectively control the deposition process. As ZIF-8 has a moderate crystal growth rate, it can be easily deposited on GO to form sandwich-like ZIF-8/GO/ZIF-8 composites *via* coordination interactions between the metal cluster from ZIF-8 and the oxygen groups from GO. Due to the similar crystal structure and unit cell parameter, ZIF-67 can be

selectively deposited on ZIF-8 seeds to form a core–shell structured MOF.

Due to the uniform deposition of core–shell structured ZIF-8@ZIF-67 crystals on the GO sheets, the obtained GO/MOF composites could be a good precursor to fabricate high-performance carbon-based catalysts for the ORR. To synthesize carbon materials, GO/ZIF-8@ZIF-67 was treated at 900 °C in Ar followed by acid etching with 2 M HCl to remove exposed cobalt nanoparticles. The sample is denoted as GO/ZIF-8@ZIF-67-900. After the carbonization process, the GO was converted to reduced GO (rGO), while ZIF crystals were converted to metal/carbon nanoparticles on rGO. The SEM images of GO/ZIF-8@ZIF-67-900 show that the nanosheet morphology is retained after high-temperature carbonization and the acid etching process, indicating that the MOF/GO/MOF sandwich-like nanostructure is thermally stable (Fig. S6†). This could be ascribed to the dense layer of MOF nanocrystals, which can retard the restack and agglomeration of GO during the carbonization process. The TEM images of GO/ZIF-8@ZIF-67-900 reveal that the cobalt nanoparticles are embedded in the carbon nanosheets (Fig. 3a). As cobalt nanoparticles can be easily removed during the acid etching process using 2 M HCl solution, these cobalt nanoparticles loaded in the carbon could be protected by the carbon matrix. The high-resolution TEM image further proves that these cobalt nanoparticles are encapsulated by a few layers of graphitic carbon (Fig. 3b and S7†). As the cobalt nanoparticles are fully wrapped by the carbon layers, the acid solution cannot make contact with cobalt species directly to dissolve the cobalt nanoparticles. The element mapping results prove that the nitrogen atoms from 2-methylimidazole ligands are doped in the carbon uniformly (Fig. 3c–f). The XRD patterns of GO/ZIF-8@ZIF-67-900 reveal four peaks, which can be ascribed to the (002) diffractions of graphitic carbon and the (111), (200) and (220) diffractions of the cobalt crystal with face-centered cubic (fcc) symmetry from the cobalt nanoparticles (Fig. S8†). X-ray photoelectron spectroscopy (XPS) of GO/ZIF-8@ZIF-67-900 shows the existence of C, N, O and Co elements on the surface of the composites, which is consistent with the element mapping results (Fig. 4a). The high-solution XPS spectrum of N 1s can be fitted with two peaks at about 398.62 and 400.67 eV, which are assigned to pyridinic and graphitic nitrogen (Fig. 4b and c).[42] Their relative contents are 56.58 and 43.42 at%, respectively. The high relative content of pyridinic nitrogen doped in the carbon is desirable as the pyridinic nitrogen could form the active sites (N–C) solely or coordinate with cobalt atoms to form Co–N_x–C active sites for the efficient ORR.[46–48] The high-solution XPS spectrum of C 1s reveals that the dominated peak positioned at 284.58 eV is attributed to the C=C bond while the peaks at 285.24 and 287.25 eV are ascribed to the C=N/C–O and C–N/C=O bonds, respectively (Fig. S9†). The N_2 sorption isotherms of GO/ZIF-8@ZIF-67-900 show that the Brunauer–Emmett–Teller (BET) surface area and pore volume are 472 m^2 g^{-1} and 1.6 cm^3 g^{-1}, respectively (Fig. 4d).

For comparison, GO/ZIF-67-derived carbon composites (denoted as GO/ZIF-67-900) were also synthesized using the same method. The XRD patterns of GO/ZIF-67-900 show typical peaks from graphitic carbon and cobalt, indicating the same compositions as those of GO/ZIF-8@ZIF-67-900 (Fig. S8†). The XPS spectrum of GO/ZIF-67-900 also reveals the existence of C, N, O and Co on the surface of materials. However, the N/C ratio of GO/ZIF-67-900 (2.7 at%) is much lower than that of GO/ZIF-8@ZIF-67-900 (8.5 at%) calculated from the XPS results (Fig. 4c and S10†). As is known, the cobalt species is a good catalyst to catalyze the graphitization process of amorphous carbon. In this case, 2-methylimidazole ligands from the MOF

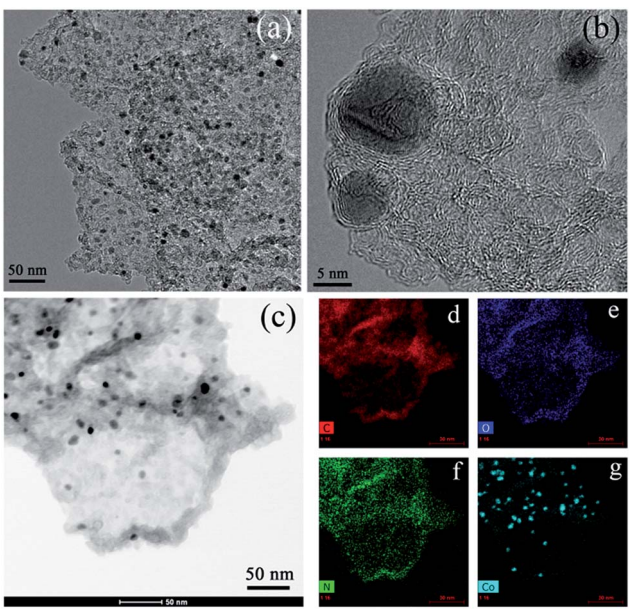

Fig. 3 TEM (a–c) and the corresponding element mapping (d–g) images of GO/ZIF-8@ZIF-67-900 prepared by carbonization of GO/ZIF-8@ZIF-67 at 900 °C followed by acid etching.

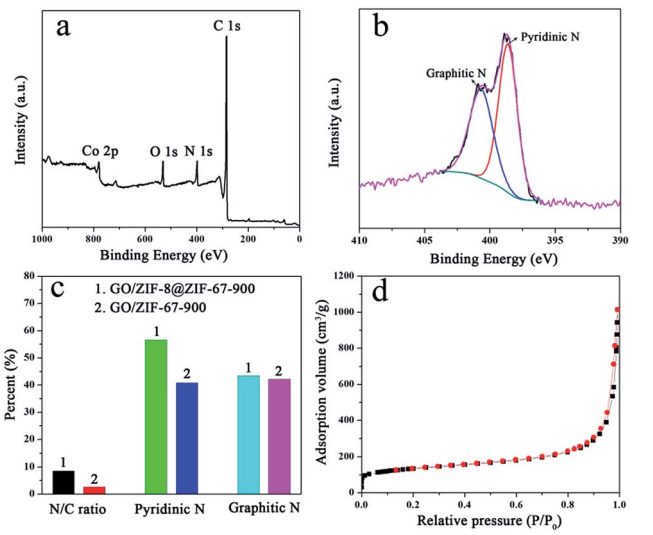

Fig. 4 (a) XPS spectrum and (b) high-resolution N 1s spectrum of GO/ZIF-8@ZIF-67-900. (c) N/C ratio, the relative content of pyridinic N and graphitic N in GO/ZIF-8@ZIF-67-900 and GO/ZIF-67-900. (d) N_2 sorption isotherms of GO/ZIF-8@ZIF-67-900.

(both ZIF-8 and ZIF-67) would be converted to amorphous carbon and then to graphitic carbon during the carbonization process with the existence of cobalt species. The graphitization process of 2-methylimidazole ligands would lead to the decomposition of the C–N bonds from the ligands, resulting in a low N content. As the MOF crystals from GO/ZIF-8@ZIF-67-900 contain both Zn and Co species, the ratio of cobalt species in the MOF is less than that of GO/ZIF-67-900. As a result, large numbers of the C–N bonds in the core–shell structured ZIF-8@ZIF-67 could be retained during the carbonization process. This result is also consistent with the previous reports.[42] The (002) diffraction peak of GO/ZIF-67-900 is also sharper than that of GO/ZIF-8@ZIF-67-900, which proves that the high content of Co species in GO/ZIF-67-900 is beneficial to the graphitization of ligand-derived carbon. The Raman spectra also show that the GO/ZIF-67-900 has a higher graphitization degree than GO/ZIF-8@ZIF-67-900 (Fig. S11†). In addition, the ratio of pyridinic nitrogen in GO/ZIF-8@ZIF-67-900 (56.58 at%) is higher than that in GO/ZIF-67-900 (40.75 at%), which is directly related to the catalytic active sites of the ORR (Fig. 4c). The BET surface area of GO/ZIF-67-900 is 485 $m^2 g^{-1}$, which is similar to that of GO/ZIF-8@ZIF-67-900 (Fig. S12†). However, GO/ZIF-8@ZIF-67-900 shows a larger pore volume than GO/ZIF-67-900 (1.0 $cm^3 g^{-1}$), which is possibly ascribed to the macropores formed by carbon nanosheets.

The ORR performance of GO/MOF-derived catalysts was evaluated using a rotating disk electrode technique. Cyclic voltammetry (CV) curves of all the cobalt/carbon composites synthesized at different carbonization temperatures using GO/ZIF-8@ZIF-67 as a precursor reveal a clear oxygen reduction peak in the O_2-saturated KOH (0.1 M) solution, indicating the electrocatalytic activity of the ORR (Fig. 5a and S13†). Here, GO/ZIF-8@ZIF-67-900 was selected as a typical catalyst for further investigation due to the slightly superior performance among these catalysts obtained at different carbonization temperatures. The CV curves of Pt/C (20 wt%, Sigma-Aldrich), GO/ZIF-8@ZIF-67-900, GO/ZIF-67-900 and GO/ZIF-8-900 exhibit the oxygen reduction peaks at 0.81, 0.82, 0.79 and 0.63 V (*vs.* the RHE), respectively (Fig. 5a and S14†). A high potential of GO/ZIF-8@ZIF-67-900 indicates high catalytic activity. The linear scan voltammogram (LSV) curves of Pt/C, GO/ZIF-8@ZIF-67-900, GO/ZIF-67-900 and GO/ZIF-8-900 at a rotating speed of 1600 rpm in O_2-saturated KOH (0.1 M) solution show that their onset potentials are 0.92, 0.93, 0.89 and 0.84 V (*vs.* the RHE) with the same catalyst loading (~0.1 mg cm^{-2}), respectively (Fig. 5b). The limiting current densities calculated based on the geometrical area of the rotating disk electrode are 5.0, 4.7, 4.3 and 3.1 mA cm^{-2} at 0.60 V (*vs.* the RHE) for Pt/C, GO/ZIF-8@ZIF-67-900, GO/ZIF-67-900 and GO/ZIF-8-900, respectively. GO/ZIF-8@ZIF-67-900 shows a higher onset potential and limiting current density than both GO/ZIF-67-900 and GO/ZIF-8-900, indicating a higher catalytic performance. Importantly, GO/ZIF-8@ZIF-67-900 even reveals a slightly higher onset potential than Pt/C at the same loading (0.1 mg cm^{-2}), further proving the high catalytic activity of this kind of nonprecious metal catalyst from GO/core–shell structured MOF composites.

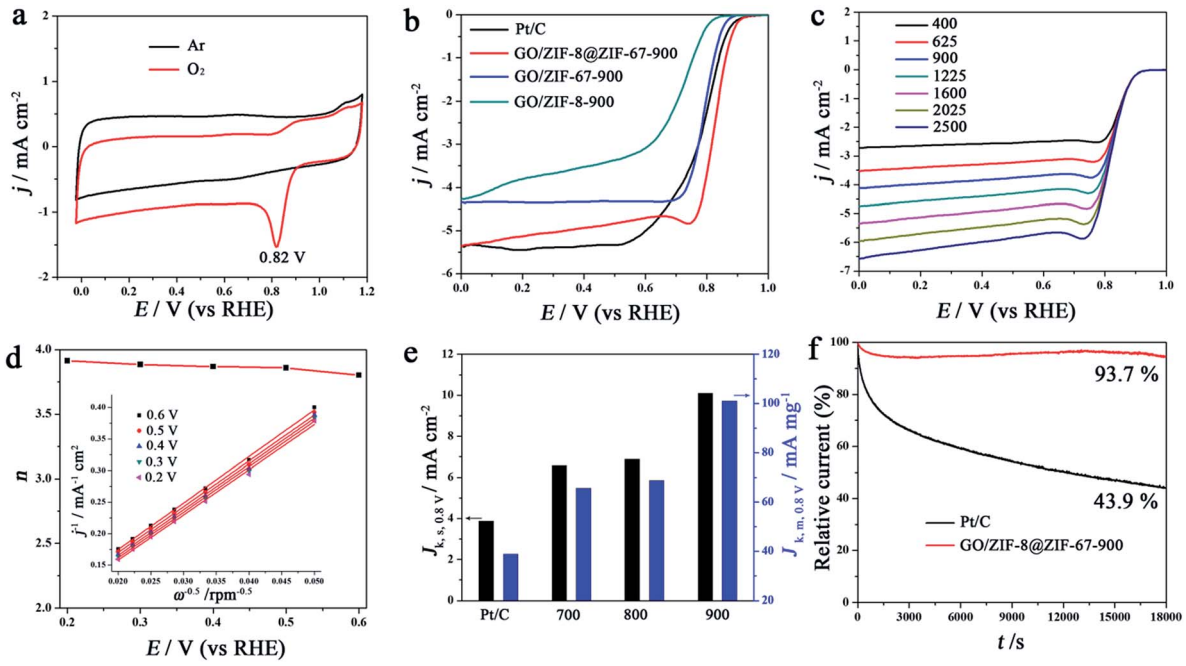

Fig. 5 (a) CV curves of GO/ZIF-8@ZIF-67-900 recorded in Ar (or O_2)-saturated KOH solution (0.1 M). (b) LSV curves of Pt/C, GO/ZIF-8@ZIF-67-900, GO/ZIF-67-900 and GO/ZIF-8-900 at 1600 rpm in O_2-saturated KOH solution (0.1 M). (c) LSV curves of GO/ZIF-8@ZIF-67-900 at different rotating speeds (400–2500 rpm); (d) electron transfer number of GO/ZIF-8@ZIF-67-900. The insets are K–L plots at different potentials. (e) The kinetic current density normalized to both the geometrical electrode surface area (black) and mass of the catalysts (blue) measured at 0.80 V (*vs.* the RHE). (f) Current–time chronoamperometric response of Pt/C and GO/ZIF-8@ZIF-67-900 at 0.80 V (*vs.* the RHE) with a rotating speed of 1600 rpm in O_2-saturated KOH solution (0.1 M). The loading of catalysts is 0.1 mg cm^{-2} for all the samples.

The electron transfer number per oxygen molecule (n) for the ORR was calculated from the LSV curves at different rotating speeds (Fig. 5c). As the rotating speeds increase from 400 to 2500 rpm, the limiting current densities increase and onset potential remains the same. The Koutecky–Levich (K–L) plots of GO/ZIF-8@ZIF-67-900 in the potentials from 0.2 to 0.6 V (*vs.* the RHE) show good linearity and a similar slope, indicating first-order reaction kinetics and a similar electron transfer number (Fig. 5d). The n for GO/ZIF-8@ZIF-67-900 is 3.8–3.9, indicating a dominant 4e pathway for the ORR.

The cobalt/carbon composites derived from GO/core–shell structured MOF composites with different molar ratios of Co to Zn were also investigated as catalysts for the ORR (Fig. S15†). All the catalysts derived from GO/core–shell structured MOF composites show better catalytic performance than those from GO/ZIF-67 or GO/ZIF-8, further proving the advantage of the core–shell structure.

As both GO/ZIF-8@ZIF-67-900 and GO/ZIF-67-900 are cobalt nanoparticles/N-doped carbon composites, and they even show similar BET surface areas (*i.e.* 472 $m^2 g^{-1}$ for GO/ZIF-8@ZIF-67-900 and 485 $m^2 g^{-1}$ for GO/ZIF-67-900), the catalytic activity of GO/ZIF-8@ZIF-67-900 is obviously better than that of GO/ZIF-67-900. This proves that the unique core–shell MOF structure is beneficial to the catalytic performance. ZIF-8 crystals act as a seed, which can facilitate the uniform deposition of ZIF-67 crystals on GO and decrease the overall crystal size of the core–shell structured MOF. As a result, more MOF (ZIF-8@ZIF-67) crystals can be deposited on the GO sheet, which could increase the density of active sites on the reduced GO after carbonization. Moreover, the core–shell ZIF-8@ZIF-67 crystals show a lower ratio of cobalt atoms than ZIF-67 with pure cobalt ions in the framework, which could partially prevent the decomposition of C–N bonds during the graphitization process, resulting in a high content of N doped in carbon. The high content of N in the carbon materials could form more active sites, resulting in an enhanced performance.

GO/ZIF-8@ZIF-67 and GO/ZIF-8 show a similar ZIF/GO/ZIF sandwich-like structure. However, GO/ZIF-8@ZIF-67-900 shows superior catalytic performance than GO/ZIF-8-900 and the carbon nanosheets from GO/ZIF-8 synthesized under the optimized conditions reported previously (Table S1†).[38] Both the core–shell structured ZIF-8@ZIF-67 and ZIF-8 nanocrystals are deposited on the GO sheet uniformly. Their derived carbon materials would show a high density of catalytic active sites. However, the cobalt species from the ZIF-67 shell of GO/ZIF-8@ZIF-67 could increase the degree of graphitization and form more efficient Co–N_x–C active sites (compared with metal-free N-doped carbon derived from GO/ZIF-8). In addition, the cobalt nanoparticles encapsulated by a few layers of graphite could also enhance the catalytic performance.[49–52] As far as we have known, it's the first example to use core–shell structured MOF/GO composites as a new kind of precursor for the synthesis of highly efficient electrocatalysts.

The kinetic current densities normalized to both the geometrical electrode surface area ($J_{k,s}$) and the mass of the catalysts ($J_{k,m}$) at 0.80 V (*vs.* the RHE) for Pt/C, GO/ZIF-8@ZIF-67-700, GO/ZIF-8@ZIF-67-800 and GO/ZIF-8@ZIF-67-900 are further investigated. GO/ZIF-8@ZIF-67-900 shows the highest $J_{k,s}$ (10 mA cm^{-2}) and $J_{k,m}$ (101 mA mg^{-1}), which are much higher than those of Pt/C (4 mA cm^{-2} and 39 mA mg^{-1}). It should be noted that GO/ZIF-8@ZIF-67-900 shows an ultra-high $J_{k,m}$ (101 mA mg^{-1}), which is higher than the recently developed catalysts such as CNT/HDC-1000 (14 mA mg^{-1})[53] and FP-Fe-TA-N-850 (32 mA mg^{-1}).[51] The high mass activity of GO/ZIF-8@ZIF-67-900 is due to the unique nanosheet structure, and high density of active sites distributed on the reduced graphene oxide. The durability of GO/ZIF-8@ZIF-67-900 and Pt/C was investigated *via* current–time chronoamperometric measurements. After 18 000 s of continuous operation, the retention of the initial current for GO/ZIF-8@ZIF-67-900 is 93.7%, which is much higher than that for Pt/C (43.9%), indicating high stability under the alkaline conditions.

The ORR performance of GO/ZIF-8@ZIF-67-900 under the acidic conditions is further investigated (Fig. S16†). GO/ZIF-8@ZIF-67-900 also obviously shows an oxygen reduction peak at a potential of 0.64 V (*vs.* the RHE), which is 150 mV lower than that of Pt/C. LSV curves of GO/ZIF-8@ZIF-67-900 show that the onset potential and limiting current density at 0.4 V (*vs.* the RHE) are 0.81 V (*vs.* the RHE) and 5.1 mA cm^{-2}, respectively. The electron transfer number is about 3.9–4.0, indicating a dominant 4e pathway for the ORR. In addition, GO/ZIF-8@ZIF-67-900 shows better durability than Pt/C under the acidic conditions. GO/ZIF-8@ZIF-67-900 is among the best of nonprecious metal catalysts reported to date under both alkaline and acidic conditions (Tables S1 and S2†). The high catalytic performance of GO/ZIF-8@ZIF-67-900 is ascribed to the following advantages. First, the MOF/GO/MOF sandwich-like nanosheets are an excellent precursor to fabricate the N-doped carbon/graphene/N-doped carbon nanostructure, which facilitate the fast mass transport and electron transfer required by the ORR. Secondly, the high density of small ZIF crystals deposited on GO could lead to carbon materials with a high density of active sites (such as N-doped C and Co–N–C). Thirdly, the cobalt/carbon composites derived from core–shell structured ZIF-8@ZIF-67 crystals combine the advantages of both ZIF-8-derived carbon (such as high N content) and ZIF-67-derived carbon (such as high graphitization degree and highly efficient Co–N–C active sites). As a result, cobalt/carbon composites with high content of N doping, good conductivity and plenty of active sites were fabricated using the GO/core–shell structured MOF as a precursor.

Conclusions

In summary, we develop a ZIF-8 seed-mediated deposition route to synthesize MOF/GO/MOF sandwich-like nanosheets with core–shell structured MOF (ZIF-8@ZIF-67) crystals distributed on GO uniformly. Due to the moderate growth rate of ZIF-8 and metal–oxygen binding between ZIF-8 and GO, ZIF-8 nanocrystals can be readily deposited on GO uniformly. ZIF-8 crystals are further used as seeds to mediate the deposition process of ZIF-67 owing to their similar crystalline structure and unit cell parameter. By contrast, ZIF-67 directly deposited on GO shows a large crystal size and inhomogeneous distributions on GO due

to the fast growth kinetics of ZIF-67. This ZIF-8 seed-mediated deposition route opens an avenue to deposit different kinds of MOF crystals on various substrates, especially for those MOF crystals with fast growth kinetics. The core–shell structured ZIF-8@ZIF-67/GO nano-sandwiches are further proved to be an excellent precursor to fabricate a highly-efficient cobalt/N-doped carbon-based catalyst for electrochemical oxygen reduction reactions. As the core–shell structured ZIF-8@ZIF-67 on GO combines the advantages of both ZIF-8 and ZIF-67, and their derived catalysts show higher catalytic performance than those derived from GO/ZIF-8 and GO/ZIF-67. We believe that this strategy using core–shell structured MOFs as precursors can be applied for the synthesis of many other functional materials and offers an alternative route to fabricate novel MOF-derived materials for the applications of energy conversion and storage.

Acknowledgements

J. Wei and Y. X. Hu contribute equally to this work. This work was supported by the Australian Research Council through Discovery grants (Project No. DP150100765 and DP150102044), Xi'an Jiaotong University through "Young Talent Support Plan" and the Foundation of State Key Laboratory of Coal Conversion (Grant J15-16-605). The authors thank the staff of Monash Centre for Electron Microscopy for their technical assistance in SEM and TEM. We acknowledge the use of equipment, scientific and technical assistance of the WA X-Ray Surface Analysis Facility, funded by the Australian Research Council LIEF grant (LE120100026).

Notes and references

1 Y. Zhai, Y. Dou, D. Zhao, P. F. Fulvio, R. T. Mayes and S. Dai, *Adv. Mater.*, 2011, **23**, 4828–4850.
2 Y. Zheng, J. Liu, J. Liang, M. Jaroniec and S. Z. Qiao, *Energy Environ. Sci.*, 2012, **5**, 6717–6731.
3 D. W. Wang and D. Su, *Energy Environ. Sci.*, 2014, **7**, 576–591.
4 J. Tang, J. Liu, N. L. Torad, T. Kimura and Y. Yamauchi, *Nano Today*, 2014, **9**, 305–323.
5 J. Liu, N. P. Wickramaratne, S. Z. Qiao and M. Jaroniec, *Nat. Mater.*, 2015, **14**, 763–774.
6 J. Wei, D. Zhou, Z. Sun, Y. Deng, Y. Xia and D. Zhao, *Adv. Funct. Mater.*, 2013, **23**, 2322–2328.
7 L. Dai, Y. Xue, L. Qu, H. J. Choi and J. B. Baek, *Chem. Rev.*, 2015, **115**, 4823–4892.
8 J. Feng, F. Pu, Z. Li, X. Li, X. Hu and J. Bai, *Carbon*, 2016, **104**, 214–225.
9 Z. Li, X. Li, Y. Zong, G. Tan, Y. Sun, Y. Lan, M. He, Z. Ren and X. Zheng, *Carbon*, 2017, **115**, 493–502.
10 X. Zheng, J. Feng, Y. Zong, H. Miao, X. Hu, J. Bai and X. Li, *J. Mater. Chem. C*, 2015, **3**, 4452–4463.
11 X. Liu, D. Zhan, D. Chao, B. Cao, J. Yin, J. Zhao, Y. Li, J. Lin and Z. Shen, *J. Mater. Chem. A*, 2014, **2**, 12166–12170.
12 X. Liu, D. Chao, Q. Zhang, H. Liu, H. Hu, J. Zhao, Y. Li, Y. Huang, J. Lin and Z. Shen, *Sci. Rep.*, 2015, **5**, 15665.
13 X. Liu, J. Liu, D. Zhan, J. Yan, J. Wang, D. Chao, L. Lai, M. Chen, J. Yin and Z. Shen, *RSC Adv.*, 2013, **3**, 11601–11606.
14 B. Liu, H. Shioyama, T. Akita and Q. Xu, *J. Am. Chem. Soc.*, 2008, **130**, 5390–5391.
15 W. Chaikittisilp, K. Ariga and Y. Yamauchi, *J. Mater. Chem. A*, 2013, **1**, 14–19.
16 W. Xia, A. Mahmood, R. Zou and Q. Xu, *Energy Environ. Sci.*, 2015, **8**, 1837–1866.
17 S. J. Yang, T. Kim, J. H. Im, Y. S. Kim, K. Lee, H. Jung and C. R. Park, *Chem. Mater.*, 2012, **24**, 464–470.
18 H. L. Jiang, B. Liu, Y. Q. Lan, K. Kuratani, T. Akita, H. Shioyama, F. Zong and Q. Xu, *J. Am. Chem. Soc.*, 2011, **133**, 11854–11857.
19 P. Zhang, F. Sun, Z. Xiang, Z. Shen, J. Yun and D. Cao, *Energy Environ. Sci.*, 2014, **7**, 442–450.
20 D. Zhao, J. L. Shui, L. R. Grabstanowicz, C. Chen, S. M. Commet, T. Xu, J. Lu and D. J. Liu, *Adv. Mater.*, 2014, **26**, 1093–1097.
21 F. Zheng, Y. Yang and Q. Chen, *Nat. Commun.*, 2014, **5**, 5261.
22 M. Zeng, Y. L. Liu, F. P. Zhao, K. Q. Nie, N. Han, X. X. Wang, W. J. Huang, X. N. Song, J. Zhong and Y. G. Li, *Adv. Funct. Mater.*, 2016, **26**, 4397–4404.
23 P. Q. Yin, T. Yao, Y. Wu, L. R. Zheng, Y. Lin, W. Liu, H. X. Ju, J. F. Zhu, X. Hong, Z. X. Deng, G. Zhou, S. Q. Wei and Y. D. Li, *Angew. Chem., Int. Ed.*, 2016, **55**, 10800–10805.
24 A. Mahmood, W. H. Guo, H. Tabassum and R. Q. Zou, *Adv. Energy Mater.*, 2016, **6**, 1600423.
25 X. J. Wang, J. W. Zhou, H. Fu, W. Li, X. X. Fan, G. B. Xin, J. Zheng and X. G. Li, *J. Mater. Chem. A*, 2014, **2**, 14064–14070.
26 B. Y. Xia, Y. Yan, N. Li, H. B. Wu, X. W. David Lou and X. Wang, *Nat. Energy*, 2016, **1**, 15006.
27 C. W. B. Bezerra, L. Zhang, K. Lee, H. Liu, A. L. B. Marques, E. P. Marques, H. Wang and J. Zhang, *Electrochim. Acta*, 2008, **53**, 4937–4951.
28 Z. Chen, D. Higgins, A. Yu, L. Zhang and J. Zhang, *Energy Environ. Sci.*, 2011, **4**, 3167–3192.
29 M. K. Debe, *Nature*, 2012, **486**, 43–51.
30 Q. Li, R. Cao, J. Cho and G. Wu, *Adv. Energy Mater.*, 2014, **4**, 737–740.
31 Y. Nie, L. Li and Z. D. Wei, *Chem. Soc. Rev.*, 2015, **44**, 2168–2201.
32 B. C. H. Steele and A. Heinzel, *Nature*, 2001, **414**, 345–352.
33 H. X. Zhong, J. Wang, Y. W. Zhang, W. L. Xu, W. Xing, D. Xu, Y. F. Zhang and X. B. Zhang, *Angew. Chem., Int. Ed.*, 2014, **53**, 14235–14239.
34 J. Wei, Y. Hu, Z. Wu, Y. Liang, S. Leong, B. Kong, X. Zhang, D. Zhao, G. P. Simon and H. Wang, *J. Mater. Chem. A*, 2015, **3**, 16867–16873.
35 Y. Hou, Z. H. Wen, S. M. Cui, S. Q. Ci, S. Mao and J. H. Chen, *Adv. Funct. Mater.*, 2015, **25**, 872–882.
36 X. Zhou, J. Qiao, L. Yang and J. Zhang, *Adv. Energy Mater.*, 2014, **4**, 1301523.
37 Y. Hou, T. Z. Huang, Z. H. Wen, S. Mao, S. M. Cui and J. H. Chen, *Adv. Energy Mater.*, 2014, **4**, 1220–1225.
38 J. Wei, Y. Hu, Y. Liang, B. Kong, J. Zhang, J. Song, Q. Bao, G. P. Simon, S. P. Jiang and H. Wang, *Adv. Funct. Mater.*, 2015, **25**, 5768–5777.

39 Y. Z. Chen, C. M. Wang, Z. Y. Wu, Y. J. Xiong, Q. Xu, S. H. Yu and H. L. Jiang, *Adv. Mater.*, 2015, **27**, 5010–5016.
40 B. You, N. Jiang, M. L. Sheng, W. S. Drisdell, J. Yano and Y. J. Sun, *ACS Catal.*, 2015, **5**, 7068–7076.
41 S. Gadipelli, T. T. Zhao, S. A. Shevlin and Z. X. Guo, *Energy Environ. Sci.*, 2016, **9**, 1661–1667.
42 J. Tang, R. R. Salunkhe, J. Liu, N. L. Torad, M. Imura, S. Furukawa and Y. Yamauchi, *J. Am. Chem. Soc.*, 2015, **137**, 1572–1580.
43 B. Y. Guan, L. Yu and X. W. Lou, *Energy Environ. Sci.*, 2016, **9**, 3092–3096.
44 K. S. Park, Z. Ni, A. P. Cote, J. Y. Choi, R. D. Huang, F. J. Uribe-Romo, H. K. Chae, M. O'Keeffe and O. M. Yaghi, *Proc. Natl. Acad. Sci. U. S. A.*, 2006, **103**, 10186–10191.
45 R. Banerjee, A. Phan, B. Wang, C. Knobler, H. Furukawa, M. O'Keeffe and O. M. Yaghi, *Science*, 2008, **319**, 939–943.
46 K. Gong, F. Du, Z. Xia, M. Durstock and L. Dai, *Science*, 2009, **323**, 760–764.
47 D. Guo, R. Shibuya, C. Akiba, S. Saji, T. Kondo and J. Nakamura, *Science*, 2016, **351**, 361–365.
48 M. Lefèvre, E. Proietti, F. Jaouen and J.-P. Dodelet, *Science*, 2009, **324**, 71–74.
49 D. Deng, L. Yu, X. Chen, G. Wang, L. Jin, X. Pan, J. Deng, G. Sun and X. Bao, *Angew. Chem., Int. Ed.*, 2013, **52**, 371–375.
50 W. J. Jiang, L. Gu, L. Li, Y. Zhang, X. Zhang, L. J. Zhang, J. Q. Wang, J. S. Hu, Z. Wei and L. J. Wan, *J. Am. Chem. Soc.*, 2016, **138**, 3570–3578.
51 J. Wei, Y. Liang, Y. Hu, B. Kong, G. P. Simon, J. Zhang, S. P. Jiang and H. Wang, *Angew. Chem., Int. Ed.*, 2016, **128**, 1377–1381.
52 J. Wei, Y. Liang, Y. Hu, B. Kong, J. Zhang, Q. Gu, Y. Tong, X. Wang, S. P. Jiang and H. Wang, *Angew. Chem., Int. Ed.*, 2016, **55**, 12470–12474.
53 Y. J. Sa, C. Park, H. Y. Jeong, S. H. Park, Z. Lee, K. T. Kim, G. G. Park and S. H. Joo, *Angew. Chem., Int. Ed.*, 2014, **53**, 4102–4106.